Vein fluorite U-Pb dating demonstrates post–6.2 Ma rare-earth element mobilization associated with Rio Grande rifting

Article *in* Geosphere · November 2019

DOI: 10.1130/GES02139.1

10 authors, including:

Gavin Piccione
University of California, Santa Cruz
6 PUBLICATIONS **14** CITATIONS

SEE PROFILE

Troy Rasbury
Stony Brook University
100 PUBLICATIONS **1,448** CITATIONS

SEE PROFILE

Research Paper

GEOSPHERE

GEOSPHERE, v. 15

https://doi.org/10.1130/GES02139.1

14 figures; 1 table; 1 set of supplemental files

CORRESPONDENCE: gpiccion@ucsc.edu

CITATION: Piccione, G., Rasbury, E.T., Elliott, B.A., Kyle, J.R., Jaret, S.J., Acerbo, A.S., Lanzirotti, A., Northrup, P., Wooton, K., and Parrish, R.R., 2019, Vein fluorite U-Pb dating demonstrates post–6.2 Ma rare-earth element mobilization associated with Rio Grande rifting: Geosphere, v. 15, https://doi.org/10.1130/GES02139.1.

Science Editor: Andrea Hampel
Associate Editor: Christopher J. Spencer

Received 3 March 2019
Revision received 25 May 2019
Accepted 2 October 2019

Vein fluorite U-Pb dating demonstrates post–6.2 Ma rare-earth element mobilization associated with Rio Grande rifting

Gavin Piccione [1,*], E. Troy Rasbury [1], Brent A. Elliott [2], J. Richard Kyle [2,3], Steven J. Jaret [1,4], Alvin S. Acerbo [5], Antonio Lanzirotti [5], Paul Northrup [1], Kathleen Wooton [1], and Randall R. Parrish [6]

[1] Department of Geosciences, Stony Brook University, Stony Brook, New York 11794, USA
[2] Bureau of Economic Geology, Jackson School of Geosciences, University of Texas at Austin, Austin, Texas 78713-8924, USA
[3] Department of Geological Sciences, Jackson School of Geosciences, University of Texas at Austin, Austin, Texas 78712-1101, USA
[4] Department of Earth and Planetary Sciences, American Museum of Natural History, New York, New York 10024, USA
[5] Center for Advanced Radiation Sources, Randall, Chicago, Illinois 60637, USA
[6] School of Earth and Environmental Sciences, University of Portsmouth, Portsmouth PO12UP, UK

ABSTRACT

Numerous studies have documented rare-earth element (REE) mobility in hydrothermal and metamorphic fluids, but the processes and timing of REE mobility are rarely well constrained. The Round Top laccolith in the Trans-Pecos magmatic province of west Texas, a REE ore prospect, has cross-cutting fractures filled with fluorite and calcite along with a variety of unusual minerals. Most notably among these is an yttrium and heavy rare-earth element (YHREE) carbonate mineral, which is hypothesized to be lokkaite based on elemental analyses. While the Round Top laccolith is dated to 36.2 ± 0.6 Ma based on K/Ar in biotite, U-Pb fluorite and nacrite ages presented here clearly show the mineralization in these veins is younger than 6.2 ± 0.4 Ma (the age of the oldest fluorite). This discrepancy in dates suggests that fluids interacted with the laccolith to mobilize REE more than 30 m.y. after igneous emplacement. The timing of observed REE mobilization overlaps with Rio Grande rift extension, and we suggest that F-bearing fluids associated with extension may be responsible for initial mobilization. A later generation of fluids was able to dissolve fluorite, and we hypothesize this later history involved sulfuric acid. Synchrotron spectroscopy and laser ablation–inductively coupled plasma–mass spectrometry (LA-ICP-MS) U-Pb dating of minerals that record these fluids offer tremendous potential for a more fundamental understanding of processes that are important not only for REE but other ore deposits as well.

1. INTRODUCTION

Laser ablation–inductively coupled plasma–mass spectrometry (LA-ICP-MS) has revolutionized geochemical analyses because it significantly reduces measurement time and allows for sample exploration in the form of elemental maps and sample transects. LA-ICP-MS is especially useful for making trace-element measurements on rocks with heterogeneous compositions and complex fluid histories. The ability to preserve mineral fabrics is particularly important in geochronology, where spatiotemporal records aid geologic interpretations. For complex geologic systems, such as hydrothermally or metamorphically altered rocks, detail often occurs on scales smaller than even a <200 um laser can distinguish. In these cases, pairing LA-ICP-MS with spectroscopic techniques such as Raman or synchrotron is an innovative way to assess the geochemical composition of the rocks being analyzed.

Hydrothermally altered rocks often have complicated tectonic and fluid histories that make it difficult to reconstruct the processes leading to orogenesis in the rock record. Dating these geologically complex deposits remains challenging. Geochronologic methods, including K-Ar and Ar-Ar on K-bearing vein materials; Sm-Nd on fluorite and garnet; Rb-Sr on sphalerite; U-Pb and Th-Pb on calcite and several other less abundant U-bearing phases have added considerably to constraining ore mineralization. More recently, the application of in situ techniques such as laser ablation ICP-MS and sensitive high-resolution ion microprobe (SHRIMP) has greatly expanded the scope for dating mineralization, particularly with U-Pb dating of carbonates and opal (Li et al., 2004; Pfaff et al., 2009; Burisch et al., 2017; Tan et al., 2017; Yang et al., 2017; Walter et al., 2018).

We studied a suite of hydrothermal veins that crosscut the Round Top laccolith (referred to subsequently as Round Top) in the Trans-Pecos magmatic province of west Texas. These veins contain high concentrations of trace elements such as REE and U and are heterogeneous on a micro-scale. We used a variety of microscopy and spectroscopy techniques to elucidate the mineralogy and details of REE enrichment in this important REE deposit. Based on these findings, we used LA-ICP-MS U-Pb dating of fluorite, nacrite, and calcite to place age constraints on vein formation events. The combined approaches allow us to identify at least two types of fluids that show clear relationships to REE mobilization. Pairing absolute and relative geochronology with REE patterns, we identify multiple REE remobilization events that occurred between 6 and 4 Ma. Knowledge of the timing of geochemistry of these fluids might offer clues into the specific complexing ligands and the mechanism for remobilization.

*Current address: Earth and Planetary Sciences Department, University of California at Santa Cruz, California 95064, USA

Rare-earth elements have long been used as geochemical proxies to characterize hydrothermal environments. Fractionation of REEs in the fluid phase can be traced back to geochemical processes including sorption, complexation, and coprecipitation (Bau, 1991; Bau and Moller, 1992; Lottermoser, 1992). Remobilization of REE has been documented in several suites of hydrothermally altered rocks (Gier, 1990; Ngwenya, 1994; Fan et al., 2004; van Dongen et al., 2010; Sheard et al., 2012; Genna et al., 2014; Li and Zhou, 2015; Debruyne et al., 2016; Cánovas et al., 2018). The mechanisms for REE remobilization are not well characterized (Williams-Jones et al., 2012; Li and Zhou, 2015). The use of geochronologic constraints to resolve REE remobilization paired with spectroscopic imaging techniques provides a possible framework for exploring these methods in future work.

2. GEOLOGIC SETTING

The Round Top Mountain rhyolite is part of the Sierra Blanca Complex, located within the Trans-Pecos magmatic province of west Texas (Fig. 1). The Trans-Pecos province extends to southern New Mexico to the north, the Pecos River to the east, and the Mexico-U.S. border to the west and south (Barker, 1987; Henry and McDowell, 1986; Price et al., 1987, 1990; O'Neill et al., 2017). Trans-Pecos magmatism occurred mainly 48–32 Ma and has been divided into two major phases (Henry and McDowell, 1986; Henry et al., 1989; Price et al., 1990; Rubin et al., 1993). The early phase (48–38 Ma) is characterized by numerous small, silicic-to-mafic igneous intrusions, mafic lava flows, and two minor caldera eruptions (Henry and McDowell, 1986; Price et al., 1990). The late phase (38–32 Ma) is calc-alkalic and alkalic volcanism, comprising the most voluminous episode of Trans-Pecos magmatism (Henry and Price, 1984; Henry and McDowell, 1986; Price et al., 1990). Sierra Blanca Peak and, presumably, the rest of the Sierra Blanca Complex laccoliths, including Round Top, were emplaced during the main phase of Paleogene bimodal Trans-Pecos magmatic activity at 36.2 ± 0.6 Ma (K/Ar in biotite; Henry and McDowell 1986). Absolute ages of emplacement of the four other laccoliths have not been determined, but a relative emplacement sequence can be interpreted through major- and trace-element differentiation patterns. Based on the increasing enrichment of REEs, especially the increasing ratio of heavy REEs (HREEs) to light REEs (LREEs) between the five laccoliths, Triple Hill was emplaced first, followed sequentially by Sierra Blanca, Round Top, Little Sierra Blanca, and Little Round Top (Shannon, 1986; Shannon and Goodell, 1986; Price et al., 1990; Elliott, 2018). The small differences in highly evolved compositions and rapid cooling textures suggest the timing between emplacement and duration of emplacement was relatively short.

Round Top is one of only a few known minable REE resources in the United States. Previous work on the elemental composition of mineral grains by electron microprobe indicates that the REEs in the Round Top laccolith are hosted by bastnäsite-(Ce), (Ce)-rich fluorite, yttrofluorite, xenotime-Y, zircon, aeschynite-(Ce), a Ca-Th-Pb fluoride, and possibly ancylite-(La) and cerianite-(Ce) (Rubin et al., 1987; Price et al., 1990; O'Neill et al., 2017). Based on the anhedral and interstitial nature of the REE-bearing trace phases, they appear to crystallize late in the history of the laccolith (O'Neill et al., 2017). Additionally, synchrotron X-ray absorption fine structure spectroscopy (EXAFS) of the Round Top rhyolite has been used to suggest that virtually all the yttrium, a proxy for the chemical speciation of HREEs, is hosted in yttrofluorite (Bau and Dulski, 1995; Pingitore et al., 2014; Ponnurangam et al., 2015). Laccolith-hosted yttrofluorite is anhedral and interstitial in nature, suggesting that it crystallized late in the petrogenetic sequence. Yttrofluorite occurs along the outer portion of feldspar phenocrysts, within K-feldspar overgrowths, as inclusions, and within the K-feldspar portion of the rhyolite groundmass (O'Neill et al., 2017). Crosscutting fractures have mineral cements including fluorite and calcite.

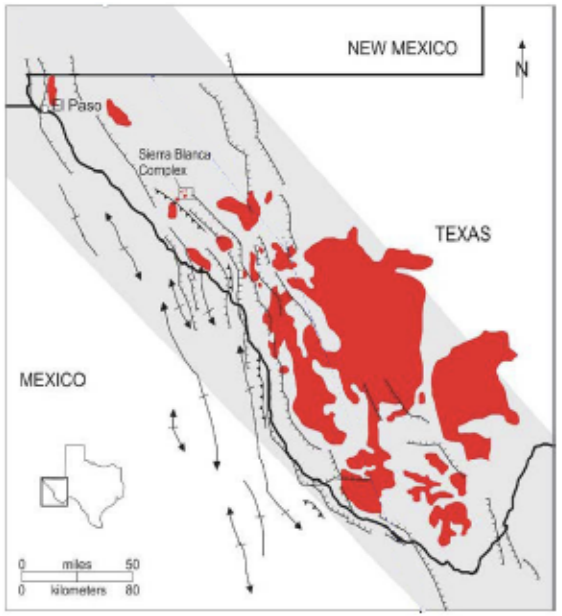

Figure 1. Location of the Sierra Blanca Complex (shown in red) relative to major geologic structures within the Trans-Pecos magmatic province. The gray shaded region represents the Texas lineament zone—a broad, ~80-km-wide zone of parallel transtensional faulting. Northwest-trending normal faults are related to Rio Grande rifting. Map modified from Muehlberger (1980), Price et al. (1990), and O'Neill et al. (2017).

Northwest-trending normal faults from Basin and Range extension dissect the Trans-Pecos region. Faults of similar orientation cut the Round Top laccolith (Fig. 1). Recent work on the Rio Grande rift suggests near synchronous rifting along the entire length between 25 and 10 m.y. ago (Ricketts et al., 2016). Based on basin subsidence, rifting was rapid until 8 Ma, followed by a significant hiatus coincident in time with Great Plains tilting at 6±4 Ma (van Wijk et al., 2018). It is suggested that the tilting and uplift are associated with a mantle

upwelling and the rate of extension has remained similar since this tilting (van Wijk et al., 2018). A compilation of strain rates across the western United States shows extension in the region beginning ca. 20 Ma and continuing to the present with important transtension between 12 and 4 Ma (Bahadori et al., 2018). Melt inclusions in olivine from basalts of the Rio Grande rift show an east to west decrease in volatiles particularly in the southern Rio Grande rift (Rowe et al., 2015). Changes in volatile budgets through time appear to reflect increasingly important asthenosphere sources following the loss of the Precambrian lithosphere (Rowe et al., 2015).

3. ANALYTICAL METHODS

We collected samples from an ~10-m-wide highly brecciated zone within one of these fault zones (pictured in Supporting Materials 1[1]). Samples were taken from within a mineralized zone that had a variety of textures with evidence for brecciation and dissolution followed by new generations of mineral formation. The vein material was found within a powdery, disaggregated matrix, and the orientations of the vein materials were not likely primary.

3.1 Sample Preparation

Samples were slabbed and polished into approximately cm-sized, mm-thick wafers for scanning electron microscopy (SEM), synchrotron X-ray spectromicroscopy, Raman spectroscopy, and laser ablation analyses.

3.2 Elemental Microscopy

Scanning electron microscopy imaging and element dispersive spectra (EDS) analyses were performed at Stony Brook University (SBU) Material Sciences facility with a Zeiss LEO1550 SEM. Samples were gold coated twice with 3 nm (6 nm total) at an angle of 30° using an Edwards 150B ES sputter coater. Samples were mounted together, and copper tape was placed across samples to prevent charging of the surface. Images were collected with a Robinson backscatter detector (RBSD) and a beam energy of 20 keV. The EDS and EDAX spectra were collected from an EDAX Phoenix sapphire detector, using software and electronics from iXRF Systems.

3.3 Raman Spectroscopy

Micro-Raman spectroscopy was conducted at the Center for Planetary Exploration (CPEX) at SBU. We used a WITec alpha300 R confocal imaging system equipped with 532 nm Nd:YAG (neodymium-doped yttrium aluminum garnet; Nd:$Y_3Al_5O_{12}$) laser with 5 mW nominal power at the sample surface and a 50× (NA = 0.8) objective (spot size of 763 nm). Spot analyses consisted of 240 1-second integrations, which were averaged. Micro-Raman maps consist of 75 × 75 µm areas acquired with 150 × 150 points per line and integration times of 0.3 seconds. Removal of cosmic rays and visualization were done within the WITec Control4 software.

3.4 Synchrotron XRF Spectromicroscopy

Initial micro-focused synchrotron X-ray fluorescence (S-XRF) imaging was performed at the X-ray microprobe beamline X26A, at the National Synchrotron Light Source (NSLS), Brookhaven National Laboratory. Mapping was conducted using a monochromatic X-ray beam tuned to 18 keV using a Si(111) channel-cut monochromator. Monochromatic X-rays were focused to a beam size of 5 × 8 µm (V × H) using a pair of 100-mm-long, elliptically bent, Rh-coated silicon mirrors in a Kirkpatrick-Baez geometry. Photon flux at this incident beam energy was ~3 × 10^9 photons per second. X-ray fluorescence spectra were collected using two single-element Vortex-EX silicon-drift-diode detectors and one four-element Vortex-ME4 silicon-drift-diode detector (SII NanoTechnology). Compositional maps were collected in a continuous scan mode as described in Lanzirotti et al. (2010).

Follow-up synchrotron XRF elemental imaging was performed at the submicron-resolution X-ray spectroscopy (SRX) and X-ray fluorescence microprobe (XFM) beamlines at the National Synchrotron Light Source II (NSLS-II), as well as the beamline 13-ID-E at the advanced photon source (APS). At the SRX beamline, samples were mounted at 35° to incident beam, while a three-element silicon-drift-diode detector was placed at 90° relative to the incident beam. XRF maps were collected by raster scanning samples through the micro-focused beam with a spot size of 2 × 2 µm. At the X-ray fluorescence microprobe (XFM) beamline, a large XRF map was collected with the sample mounted at 45° relative to the micro-focused incident beam with a spot size of 5 × 8 µm. Data were collected using on-the-fly scanning with a 125 ms dwell time using a four-element Vortex-ME4 silicon-drift-diode detector with incident energy tuned to 17.3 keV. At beamline 13-ID-E, samples were mounted at 45° relative to the incident beam, and samples were raster scanned with a micro-focused spot size of 1 × 1 µm. X-ray fluorescence was measured with an incident beam energy to two different energies above and below the U L-edge binding energy, 17.08 and 17.18 keV, using a four-element silicon-drift-diode detector (Hitachi) mounted at 90° relative to incident beam. Two incident beam energies, 17.08 and 17.18 keV, above and below the U L-edge binding energy, were used at 13-IDE to correct for spectral overlaps of the U L-edge emission lines with emission lines due to Rb and Sr K-edge fluorescence, which in fluorite can be very pronounced with energy dispersive analysis at the energy resolution of the detector. These overlaps are strongest on the U Lα emission line but negligible when generating maps using the U Lι.

S-XRF microprobe measurements were made in the "tender" energy range of 1 to 5 keV, at the tender energy X-ray spectroscopy (TES) beamline 8-BM and at NSLS-II and at beamline X15B at NSLS (Northrup et al., 2016; Northrup,

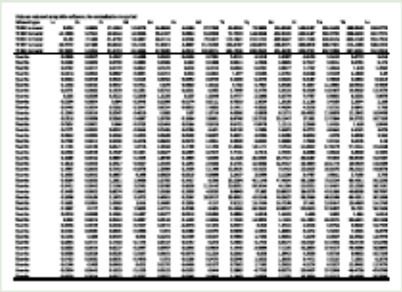

[1]Supplemental Materials. Supporting Materials 1: Outcrop photos. Data Set S1: U-Th-Pb raw data with data reduction math. Data Set S2: REE data for each mineral analyzed. Data Set S3: Metadata associated with data acquisition, processing, and reporting following Horstwood et al. (2016). Data Set S4: Compilation of WC-1 standard analyses associated with each unknown analyte. Table S1: Compilation of ages organized by sample. Please visit https://doi.org/10.1130/GES02139.S1 or access the full-text article on www.gsapubs.org to view the Supplemental Materials.

2019). Incident beam energy was set to 3555 eV with Si (111) monochromator crystals and focused to a 5 × 10 µm spot size for large elemental maps and for microbeam X-ray absorption spectroscopy and was reduced to 2 × 3 µm for fine mapping. Earlier measurements at X15B (NSLS precursor to TES) used a spot size of 10 × 15 µm and Si (111) monochromator. Samples were oriented at 45° to beam, and fluorescence was measured using a Canberra ultra-low-energy Ge detector. Setting an energy of 3555 eV stimulates fluorescence from the U M_5 edge, the Y L_3 edge, and the S, Si, Al, and Mg K-edges but is below the Ca K-edge to avoid interferences from that major element. Energy scanning was conducted in quick on-the-fly mode, 10–30 seconds per scan with multiple scans at selected pixels of the elemental maps.

3.5 Laser Ablation Element Analyses and U-Pb Geochronology

Laser ablation–inductively coupled plasma–mass spectrometry (LA-ICP-MS) analyses were conducted at the Facility for Isotope Research and Student Training (FIRST) at SBU. A 213 UV New Wave laser system coupled to an Agilent 7500cx quadrupole ICP-MS was used for the analyses. Data sets include ^{238}U, ^{232}Th, ^{208}Pb, ^{207}Pb, and ^{206}Pb isotopes, which were collected sequentially for 0.1 seconds each throughout 30 second ablations. An 80 µm spot size was used for most of the analyses (40 and 160 µm spots were also used in some of the sequences). For all of the analytical sessions, unknowns were bracketed by at least five standard spots, and two standard spots were interspersed after every five unknown spots. A typical session includes 20–30 unknowns and 16–20 standards. The WC-1 calcite standard (Roberts et al., 2017) was used as a standard of known age for all mineralogies (carbonate, fluorite, and other minerals) due to the lack of standards for these unusual minerals, and National Institute of Standards and Technology (NIST) 612 was used for Pb isotope fractionation correction and for approximating element concentrations using signal intensity ratios. Data were reduced in iolite (Paton et al., 2011) using the U-Pb Geochronology 3 (or 4) data reduction scheme for U-Pb analyses with NIST 612 as the primary Pb-U standard. Element concentrations were processed with the trace-element data reduction schemes (DRS) in semiquantitative mode using NIST 612 as the standard. These DRS subtract baselines and correct for downhole fractionation and drift of the signal.

For U-Pb LA-ICP-MS, reduced data are plotted using Isoplot (Ludwig, 1998, 2003, 2012) on a modified Tera-Wasserburg isochron plot following the procedure of Parrish et al. (2018). This method calculates radiogenic ^{208}Pb from ^{232}Th decay and then subtracts it from total ^{208}Pb to find the amount of common ^{208}Pb (208c). This value is then used in plotting $^{208}Pb/^{206}Pb$ versus $^{238}U/^{206}Pb$. Using $^{208}Pbc/^{206}Pb$ also allows for common Pb-corrected $^{238}U/^{206}Pb$ ages without having to measure ^{204}Pb. Using this plot, the age and uncertainty corresponding to the X-axis intercept were used. Individual data points were also corrected for common Pb using a Stacey-Kramers model age value of $^{208}Pb/^{206}Pb$ and plotted as a weighted average for related samples (Data Set S1 [footnote 1]). All uncertainties on age calculations were reported as 2σ.

A secondary normalization used WC-1 for calcite, fluorite, and nacrite. Although it would have been desirable to have matrix-matched standards, we make the assumption that while some bias between calcite and fluorite may exist, it is likely to be less than the ~7% demonstrated by Parrish et al. (2018) between calcite and zircon. A further potential issue in our dating is the lack of knowledge of the initial U activity ratio ($^{234}U/^{238}U$) of the U-rich fluids. High activity can lead to the presence of unsupported ^{206}Pb, which would cause age calculations to be too old. This effect has been well documented in calcite in speleothems of later Pleistocene age. However, given the mainly late Miocene and Pliocene ages of this study, it would be nearly impossible to measure any residual disequilibrium, and therefore we are unable to make any quantifiable correction for this effect. We have not added any additional uncertainty arising from these sources of potential bias because they are likely insignificant relative to the range of ages and magnitude of reported uncertainties presented here and therefore hold little potential to change the overall interpretation of ages and their geological significance. Furthermore, isochron ages presented here have a spread of mean square of weighted deviates (MSWDs) that range from under to over dispersed, with some much larger than 1. Modeled ages with over-dispersed MSWDs are treated with caution, but the ages are entirely consistent with better constrained isochrons.

4. RESULTS

4.1 Host Rhyolite Relationships to Vein Minerals within the Fracture Zone

Within the fracture zone, we find fragments of host rhyolite with and without vein minerals. Veins that cut the host rock (Figs. 2A and 2B) are filled with a mixture of nacrite and fluorite. Fragments of host rock and nacrite show in situ brecciation, and the area around the breccia clasts is filled by a white calcite cement (Figs. 2B–2D and 2G). Nacrite, which can be light purple (Figs. 2B and 2D top), pink (Fig. 2G), light green (Fig. 2D bottom), or tan (Fig. 2C), commonly forms layers that are followed by green fluorite and then white calcite (Figs. 2B–2D). As seen in Figure 2D, sometimes these layers appear to have formed on a preexisting calcite cement. A YHREE carbonate, which we hypothesize to be lokkaite but refer to henceforth as YHREE carbonate due to uncertainty in its identification, commonly occurs at boundaries between fluorite and calcite, as shown in section 4.1.3. Fluorite is also found alone (Fig. 2E) as well as in the form of brecciated clasts within white calcite matrix (Fig. 2F and 2G). Some examples of the breccia have clasts of primarily nacrite and fluorite within a white calcite cement (Fig. 2G). Calcite is the principal mineral within the fracture with a variety of geometries and types, but the most common of those is a lighter-colored calcite. Dark-brown calcite occurs both as a mixture and independent of this white calcite (Fig. 2H). There are variations on the samples shown here with fluorite and nacrite forming layers as well as clasts. We have not found calcite as clasts in the breccia. We see a

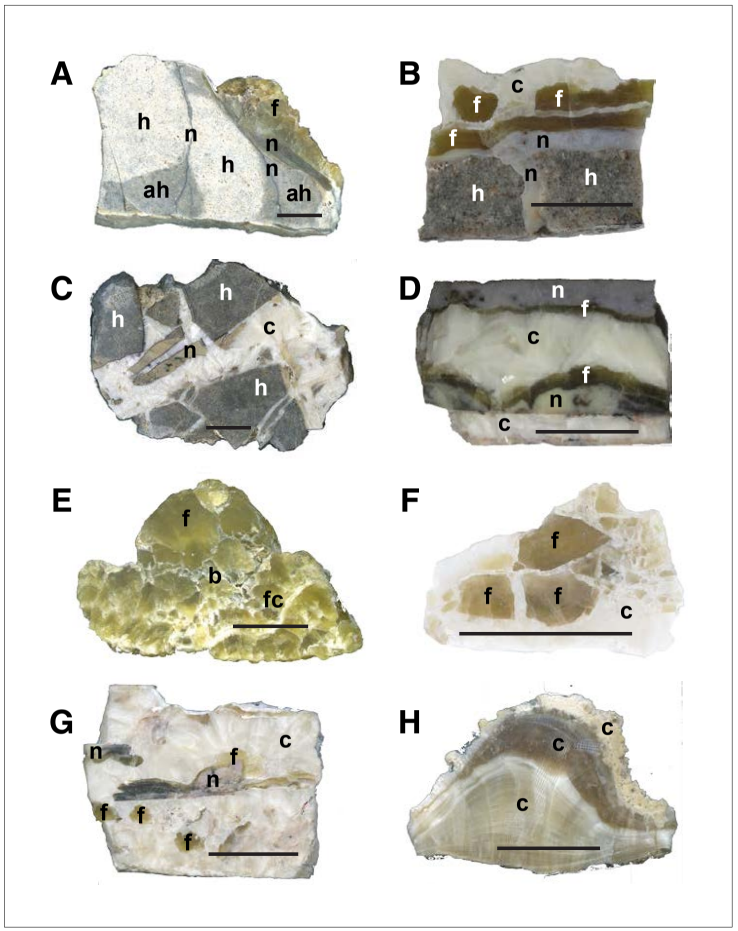

Figure2.Visiblelightimagesofthesamplesfromthefracture.(A)Hostrockwithsmallveinsthatare filledbynacriteandcappedby fluorite.(B)Fracturedhostrhyolitewithnacritebetweenfragments andonsurfacesfollowedby fluorite,whichisbrecciatedandcementedbycalcite.(C)Brecciated hostrhyoliteandnacritethatiscementedbycalcite.(D)Layeredveinmaterialwiththecalciteon thebottomappearingtobethesurfaceuponwhichnacritefollowedby fluoritefollowedbycalcite grew.Thesemineralsappeartocomefromthetopandbottom.(E)Brecciatedgreen fluoritewith calcite fillingbetweensomefragments.(F)Brecciated fluoritewithcalcitecement.(G)Breccia withnacriteand fluoriteclasts.(H)Twogenerationsofcalcite.Thewhitetoambercalciteishighly enrichedinrare-earthelements(REEs).Thebrowncalciteislowin REEbuthashighU-Pbratios. Labelsare:h– host;ah– alteredhost;n– nacrite;f– fluorite;fc– fluoritewithcalcite;c– calcite; b– brecciatedzone.Notvisiblehereistheyttriumandheavyrare-earthelement(YHREE)carbon - atethatlinesthebrecciaclastsandoccursbetween fluoriteandcalcite.Scalebarsareall1cm.

gradationbetweenlayeredsamples(Figs.2Band2D)andhighlybrecciated samples(Figs.2C,2F,and2G).Calciteappearstomineralizelast, fillingspaces andperhapsdisplacingothermineralsduringgrowthinatleastsomecases. Forexample,inFigure2B,thegreen fluoriteisfragmentedandseparatedby calciteeventhoughitformsalayerovernacrite.

4.1.1Nacrite

Ramanmappingofthemicrocrystallinephaseshown inFigures2B,2D, and2G(labelednacrite)isconsistentwithnacriteAl $_2Si_2O_5(OH)_4$withseveralstrong Ramanpeaksat126,195,318,524,747,3619,and3696 Δcm^{-1}(Figs.3Band3C). Ramanmapsareconsistentelementalchemistry,whichindicatesanAl-rich phase.Insomecases,othercations(particularlyMgandFe)arepresent,which mayindicateasolidsolutionwithdickite.Ramanspectroscopyisnotableto distinguishbetweennacriteanddickite.Here,forsimplicity,werefertothis phaseasnacrite,althoughwenotethemaybechemicalcomplexity.The peakat318 Δcm^{-1}isconsistentwith fluorite,suggestingthatthisphaseisa mixofnacrite+ fluorite(Fig.3C).Thisnacriteand fluoriteassociationisatthe submicronscale,becauseitisnotpossibletodistinguishbetweenthemat thehighestmagni ficationwiththeSEMormappingwithaRamanspotsize

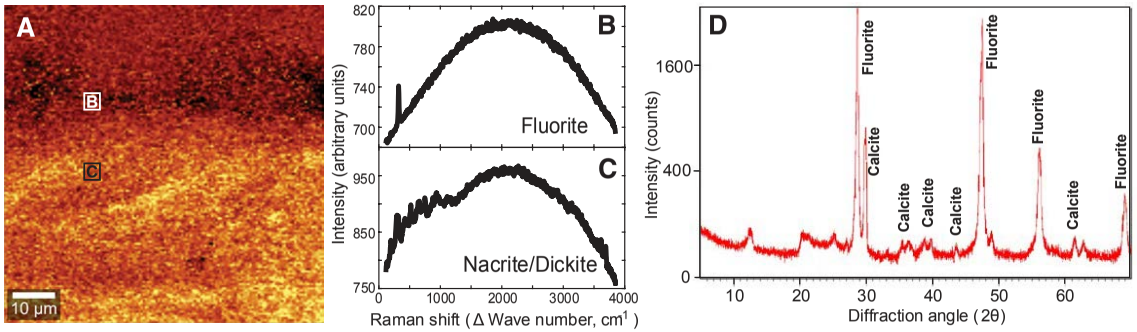

Figure 3. (A) Raman map of vein mate - rial.Darkregionontopis fluorite(spectra shownin B);lighterregiononthebottom isnacrite(spectrashowninC).(B)Raman spectraindicate fluorite.(C)Ramanspec - trafromcryptocrystallinephaseshowthe presenceofnacrite.(D)X-raydiffraction (XRD)spectraofaselectedcryptocrys - tallinephaseindicatemixtureof fluorite, calcite,andaweaklycrystallinephase(s) consistentwithnacrite.

of 763 nm (Fig. 3C), but XRD confirms the presence of fluorite in this phase (Fig. 3D; Table 1). Nacrite is found as layers and crosscutting veins within the host rhyolite and as breccia clasts within white calcite matrix. Based on cross-cutting relationships between nacrite and the host rock, as well as nacrite's relationship with fluorite and calcite, nacrite appears to be the first mineral deposited in the fracture zone. Nacrite is always associated with fluorite in these veins, both as an intimate mix and with fluorite capping it.

No finely dispersed REE phases are identifiable in the nacrite using SEM imaging. Synchrotron XRF element mapping shows areas of elevated concentrations of Y within nacrite, suggesting that it is either itself Y enriched or that it contains finely dispersed REE minerals at less than the spatial resolution of the incident beam (2 µm, Fig. 4B). Yttrium X-ray absorption near edge structure (XANES) spectra collected for enriched areas in the nacrite are indistinguishable from spectra collected from YHREE carbonate, while dissimilar from spectra collected from the host rock (Fig. 4A). It thus is likely that Y is present as a similar chemical species in both materials.

Nacrite (dickite) co-occurs with the YHREE carbonate where it lines a zone of brecciation and dissolution within fluorite (Fig. 5D). While nacrite has an intimate association with fluorite in the examples described above, this example shows it can also coexist with the YHREE carbonate independent of fluorite. The mineral is too small to be analyzed by XRD, but Raman spectroscopy confirms it is either nacrite or dickite. Scanning electron microscopy EDS analyses (and TESCAN XRF imaging) demonstrate that some (but not all) occurrences of this mineral have Mg (Figs. 5D and 5G), suggesting it is dickite. Based on microstratigraphic relationships, the clay mineral that occurs with the YHREE carbonate forms later than the green fluorite it caps.

TABLE 1. X-RAY DIFFRACTION (XRD) OF Al-Si PHASES

Sample	Fluorite (%)	Nacrite (%)	Mg-calcite (%)
Tan mineral shown in Figure 2C	70.3 (1.4)	13.3 (0.7)	16.4 (0.7)
Purple mineral shown in Figure 2D	83.6 (2.2)	16.4 (2.6)	Not detected
White mineral shown in Figure 2E	91.5 (6.1)	8.5 (6.4)	Not detected

Notes: Data were collected for two hours on a spinning stage; data were processed in X'pert Highscore Plus software; numbers are calculated percent of total as determined by spectral fitting.

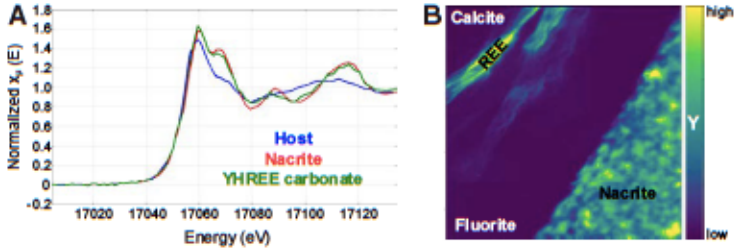

Figure 4. (A) Yttrium K-edge X-ray absorption near edge structure (XANES) (YHREE carbonate mineral–green; nacrite–red; host rock–blue). Data from submicron-resolution X-ray spectroscopy (SRX) at the National Synchrotron Light Source (NSLS) II. (B) Synchrotron X-ray fluorescence (S-XRF) map (blue– low concentration; yellow– high concentration) showing Y-rich mineral lining fluorite (rare-earth element) and Y-rich spots in the nacrite. Map dimensions are 0.2 × 0.2 mm. YHREE–yttrium heavy rare-earth element.

4.1.2 Green Fluorite

Green fluorite is a common phase within the fracture zone. It is found capping the host (Fig. 2A), as layers following nacrite (Figs. 2B and 2D), as clasts within calcite-cemented breccia (Figs. 2F and 2G), and predominantly as fluorite that can be brecciated and have calcite veins (Fig. 2E). Synchrotron XRF element mapping reveals that there are (at least) two distinct generations of similar color fluorite that are separated by a brecciated zone (Figs. 2 and 6). One generation (the top part of Figs. 2E and 6) is enriched in Sr and lower in U; the other generation (the bottom part of Figs. 2E and 6) is enriched in U and lower in Sr. The U in fluorite was determined to be in the 6+ oxidation state by U M_5-edge and L_3-edge XANES. Scanning electron microscopy element mapping reveals fragments of fluorite in the brecciated zone with evidence of dissolution (Fig. 5D). Within the brecciated zone, void surfaces (the voids are easily visualized by examining the Ca map in Fig. 6) are coated with an YHREE mineral, as shown by the Y map (Fig. 6). Physically, the two generations are distinct because the top part is clear, without obvious inclusions, while the bottom part has opaque white layers (Fig. 2E). The white layers are calcite and are discussed below in section 4.1.4.

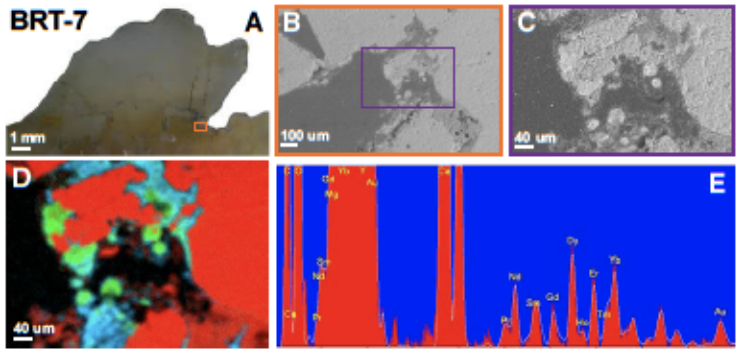

Figure 5. (A) Visible light image of brecciated green fluorite. (B) Scanning electron microscopy (SEM) image from the orange boxed area on A. (C) Further zoom on the brecciated fluorite; area indicated by the purple box in B. (D) RGB color image of area in C; red–Ca (fluorite); blue–Mg (dickite and nacrite); green– Y (YHREE-bearing carbonate). (E) Energy-dispersive X-ray (EDX) spectra of yttrium and heavy rare-earth element (YHREE) carbonate mineral. Note resorbed texture in the fluorite and the close spatial association of the YHREE mineral and dickite.

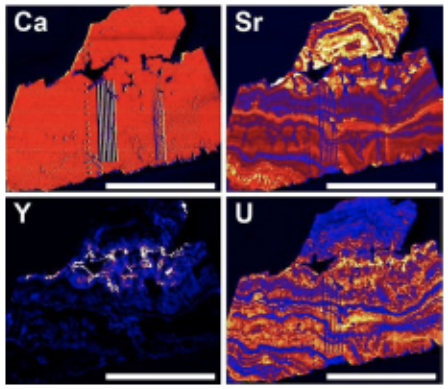

Figure 6. Synchrotron X-ray fluorescence (S-XRF) maps from X26A, National Synchrotron Light Source (NSLS). White bar is 1 cm. Lines and spots on surface are from laser ablation. Ca– calcium; Sr– strontium; Y– yttrium; and U– uranium.

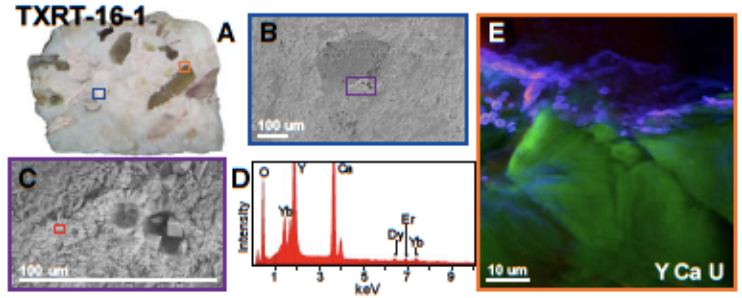

Figure 7. (A) Visible light image of vein breccia. (B) Scanning electron microscopy (SEM) image of area in blue box on A. (C) SEM image of area in purple box on B; shows nodules of yttrium and heavy rare-earth element (YHREE) mineral. (D) Energy-dispersive X-ray (EDX) spectra from area outlined by red box in C. (E) Synchrotron X-ray florescence (S-XRF) elemental image taken at 13-ID-E beamline of the edge of a fluorite clast; area of image outlined by orange box in A. RGB coloration is Y, Ca, and U, respectively.

4.1.3 YHREE Carbonate

A YHREE carbonate is found coating dissolution surfaces and lining breccia clasts. This mineral is sometimes associated with nacrite and dickite (Fig. 5D) and is often followed by calcite. A zone of brecciation and dissolution in the green fluorite provides important insight into the timing of this YHREE carbonate, precipitating after green fluorite, directly on dissolution surfaces (Figs. 5D and 6Y).

Similarly, clasts of nacrite and fluorite in breccia samples (such as shown in Figs. 2F and 2G) are coated by an YHREE carbonate mineral that is followed by white calcite (Fig. 7). Energy dispersive spectra mapping of Y shows the pervasive nature of the YHREE mineral coating clasts as well as other surfaces (Figs. 6Y and 7B±7E). The YHREE carbonate is also arranged in nodules (Fig. 7C). Based on EDS spectra, the REE mineral contains Ca, Y, C, O, and HREEs (Fig. 7D) and is most likely lokkaite [$Ca(Y,Gd,Nd,Dy)_4(CO_3)_7 \boxtimes 9H_2O$].

4.1.4 Calcite

Calcite from within the vein appears to be the latest phase, with multiple generations that may be separated by dissolution surfaces shown by the irregular contacts between generations. Many calcite samples are tabular, suggesting that they formed along fracture surfaces. Most samples have unfilled pore space between layers, suggesting calcite growth does not displace existing vein minerals or that dissolution followed growth. The layers typically show a pattern of growth that alternates between white and brown (Figs. 8A±8C). When viewed in plan view, brown calcite appears to form elongated cm-wavelength ridges on the surface (Fig. 8A). These ridges are underlain by mounded brown calcite (Fig. 8A), suggesting its formation and possibly dissolution are responsible for the ridges. The brown calcite is capped by a spongy tan calcite that appears to be a residue (Fig. 8A). When polished, the white calcite appears to be more amber with white layers (Figs. 8B and 8C). These white layers have elevated Y (Fig. 8C), while the overlying brown calcite has low Y and high U (Fig. 8C).

With SEM imaging, we observed the YHREE carbonate on the irregular surface at the base of the white calcite shown in Figure 8. Synchrotron XRF maps show the REE coating the calcite surface (Fig. 8D). The REE and Y are also elevated in the white layers of the calcite as shown by LA element maps (Fig. 8C). Synchrotron XRF maps show that some REEs occur as discrete phases within the calcite (Fig. 8E). The S-XRF element map also reveals the brecciated nature of the REE-enriched contact between white and brown calcite (Fig. 8E).

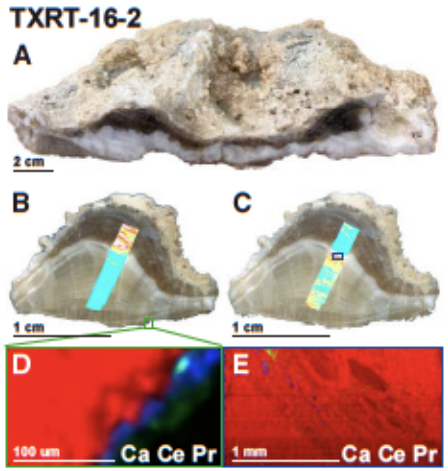

Figure 8. (A) Visible light photo of vein as shown in Figure 2H. (B) Cross section of slab cut from sample in A. Laser ablation map of U concentration (hot colors = high; cold colors = low). (C) Cross section of slab cut from sample in A. Laser ablation map of yttrium (Y) concentration (hot colors = high; low colors = low). (D, E) Composite RGB X-ray fluorescence (XRF) elemental maps taken at submicron-resolution X-ray spectroscopy (SRX); area corresponding to green and purple boxes in B and C, respectively. RGB maps are Ca, Ce, and Pr, respectively.

Scanningelectronmicroscopyimagingand S-XRFmappingwithTESreveal thattheopaquewhitelayerswithinthebrecciated fluoritesample(Fig.2E)are calcite fillingdissolutionvoidsafter fluorite(Figs.9Band9C).Silicon,S,andY linedissolutionsurfaces(Figs.9Cand9D),andSiandYarehighlycorrelated (Fig.9D).Uraniumishighlyconcentratedin fluorite,andtheUmapsshow cubicshapesthatarenowskeletalthatareassociatedwithS(Figs.8Eand 9E).Elementdispersivespectraofthecalcite,athighmagni fication,without evidenceforotherphases,showthatAlandSiarepresentatthisscale(Fig.9F).

4.1.5MineralRelationshipsandREEPatterns

Westudiedasamplethatcontainsalloftherecognizedphasesdescribed abovetoilluminatemineralrelationships(Fig.10).WeusedS-XRFmapping athard(Fig.10B)andtenderenergy(Fig.10C)rangestomapCa,Al,Mg,S,Si, Y,U,andFeinthissample.AlandMgclearlydelineatenacrite(Fig.10B).By comparison,itisclearthatS,Ca,Sr,Y,andUareelevatedinnacrite(Figs.10B and10C).Uraniumishighlyelevatedbutzonedin fluorite(Figs.10Band10C). TheYHREEmineral,asillustratedbythemappatternofY,occursbetweencal - citeandnacrite(Figs.10Band10C),andbetween fluoriteandcalcite(Figs.9D and9E),butnotbetweennacriteand fluorite.

Rare-earthelementpatternsbasedonelementanalysesbyLA-ICPMSshow differencesbetweenphases.TheREEpatternsforthenacriteshowpronounced negativeCeandEuanomalies,withmiddleandheavyREEenrichmentanda humpintheMREE(Fig.11A).Green fluoritehaslowerREEconcentrationsbuta verysimilarpatterntothenacrite(Fig.11B).Calcitealsoshowsthepronounced negativeCeandEuanomalies,butitisfarmoredepletedintheLREEsand showsasteeprisetotheHREE,quitedistinctfromthenacriteand fluoriteREE patterns(Fig.11C).Insomecalcitesamples,thereisaslightincreasetohigher enrichmentintheREEheavierthanHo,perhapsduetomixingwiththeYHREE mineral(Fig.11C).Rare-earthelementpatternsobtainedonbrowncalciteshow similarpatternswithpronouncednegativeCeandEuanomaliesandHREE enrichment.Calcitecrustdoesnothaveparticularlyelevated REE,althoughit doesshowthetypicalHREEenrichmentofcalcite.TheYHREEcarbonatehas middletoheavyREEpatternswithahumpatEr(Fig.11D).SomeoftheREE elevatedareasaremoreenrichedinthelightREE.

4.2U-PbGeochronology

Fluorite,nacrite,andbrowncalcitewithinRoundTopfracturesareenriched inUandhavefavorableU-Pbratios.Therearemultiplegenerationsofallof thesephasesbasedontheirrelativeorderaswellasonthedifferencesincolor, geochemistry,andages.TraditionalTera-Wasserburgplotsyieldanalytically indistinguishableagestomodi fiedTera-Wasserburgplotsusing ^{232}Th-corrected ^{208}Pbasthenormalizingisotope.Thus,wefollowParrishetal.(2018)anduse the86TWplotandcommonPb-corrected,weighted-average ^{238}U-^{206}Pbplots.

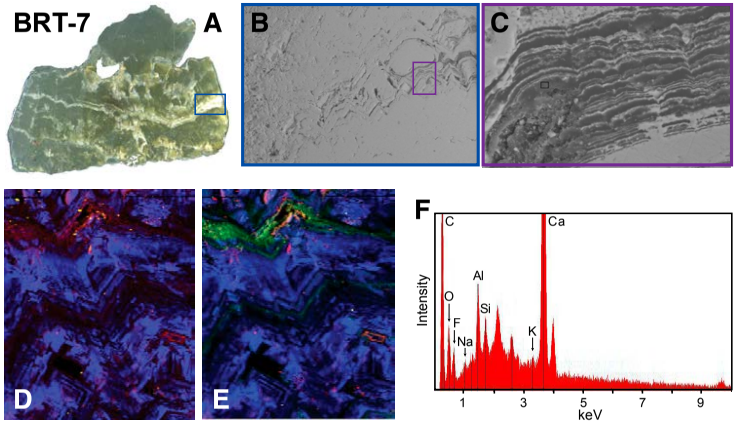

Figure9.(A)Visiblelightimageofbrecciatedgreen fluoritesampleasshowninFigure3E.(B)Scan - ningelectronmicroscopy(SEM)imagefrominsetareaoutlinedinblueboxinA.(C)SEMimage ofareaoutlinedinpurpleboxinB.(D)X15BRGBmapofY,Si,U,respectively.(E)X15BRGBmap ofY,S,andU,respectively.(F)Energy-dispersiveX-ray(EDX)spectraofcalciteshowthatAland Siarepresentevenathighmagni fication.

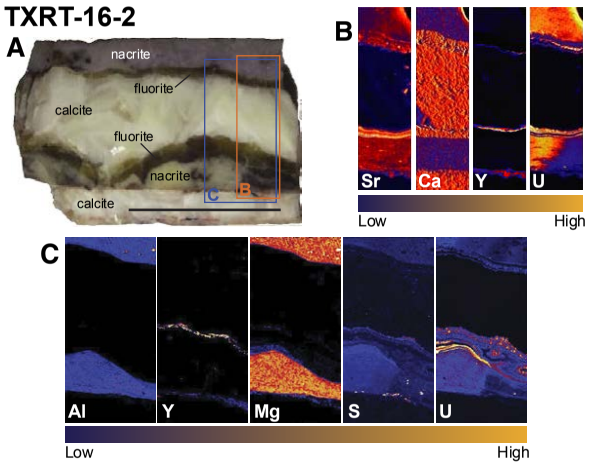

Figure10.(A)Visiblelightimageofalayeredveinasshownin Figure3D. Scalebaris1cm.(B)X-ray fluorescence(XRF)elementalmapsoftheSr K-edge,CaK-edge,YK-edge,andUL-edgetakenatX-ray fluorescencemi - croprobe(XFM)beamline;areacorrespondingtothesmallorangerectangle inA.(C)XRFelementalmapsoftheAlK-edge,YL-edge,MgK-edge,SK-edge, andUM-edgetakenatTenderEnergySpectroscopy(TES)beamline;area correspondingtothelargerpurplerectangleinA.

4.2.1Fluorite

Fluoriteismoderatelytohighlyelevatedin U,withconcentrationsof 15±1500ppm(DataSetS2[footnote1]).PbandThconcentrationsare,in mostcases,muchlowerthan1ppm.Fluoritehasarangeof $^{238}U/^{206}Pb$from 200to2024andagesthatrangefrom6.2to3.2Ma(Fig.12).Theoldestfluoriteidentifiedisdarkgreen,formsdirectlyonthehostrock(Fig.2A),and givesanageof6.2±0.4Ma(Fig.12A).Slightlyyoungeragesarefoundin thewell-studiedsampleBRT-7showninFigures2E,5,6,and9;thissample hastwogeochemicallydifferentgenerations(Fig.6).Theolderfluoritegeneration,foundonthebottomofthesampleasorientedinFigure6,givesan ageof5.5±1.1Ma(Fig.12B).Thenextoldestfluoriteformsverythincoatings ofdark-purplefluoriteonclastsofhostrock(Fig.2B);itgivesanageof5.2 ±0.1Ma(Fig.12C).Adark-greenfluoritethatfollowspurplenacriteandfluorite precipitationgivesanageof5.0±0.5Ma(Fig.12D).Greenfluoriteclastswithin calcite-cementedbreccia(Figs.2Fand2G)arethenextyoungestgeneration andgiveoverlappingagesof4.9±0.3Maand4.7±0.2Ma(Figs.12Eand12F). Alloftheaboveagesareinfactindistinguishablefromca.5Ma.Thesecond generationoffluoritefoundinthetopoftheBRT-7(Figs.2E,5,6,and9)is4.1 ±0.6Ma(Fig.12G).Adark-greenfluoritethatfollowsgreennacritegivesthe youngestfluoriteageat3.2±0.4Ma(Fig.12H).

4.2.2Nacrite

Nacriteoccursinfourdifferentcolorswithvariable U,Th,andPbconcentrations(DataSetS2[footnote1]).ThandPbconcentrationsarefarhigherthan fluorite,andthusthe $^{238}U/^{206}Pb$isgenerallylower.Theagesofnacriteoverlap withthoseoffluorite.Theoldestgenerationofnacriteistanandoccursas brecciaclastswithhostrock(Fig.2C).Thisgenerationofnacriteissurrounded byathinlayerofpurplefluoriteandgivesanindistinguishableagefromthat fluoriteof5.6±1.3Ma(Fig.13A).Apurplenacritelayerfromthesampleshown inFigure2Bclearlycrosscutsthehostrockandgivesanageof3.5±1.9Ma (Fig.13B).Anotherpurplenacritelayercappinggreenfluorite(Fig.2D)anda pinknacrite(Fig.2G)withsurroundinggreenfluoritegiveindistinguishable agesof3.4±0.4Maand3.3±1.0Ma(Figs.13Cand13D).Agreennacritelayer, alsofromFigure2D,givesaslightlyyoungerageof3.3±0.1Ma(Fig.13E). Theyoungestnacritemeasuredwasasmallgreenclastfromthesamplein Figure2G,whichgaveanageof2.8±0.6Ma(Fig.13G).

4.2.3Calcite

Calciteoccursasmultiplegenerationswithdissolutionsurfacesinbetween. Forthemostpart,thecalcitehaslowUandunfavorable $^{238}U/^{206}Pb$(DataSet S2[footnote1]).Awhitecalcitewithcurvedcrystalsmakesupthematrix materialformostoftheveinswestudiedandencasesbrecciaclasts(Figs.2F and2G).Thiscalcitehaslow UandlowU-Pbandisthereforenotsuitablefor dating;basedonrelativerelationships,itoccurslaterthanfluoriteandthe YHREEmineral.Anothercalcitesamplehasadistinctivebrowncolorandhas elevatedYandYHREEcarbonatesonitslowersurface(Fig.2H).Theelevated Y,aswellasthecolorandtexture,suggestitisaseparategenerationfrom thebreccia-cementingwhitecalcite.Thiscalcitehassomelayersofhigh U-Pb. Combined,thecalcitegivesanageof1.7±0.1Ma(Fig.13F).

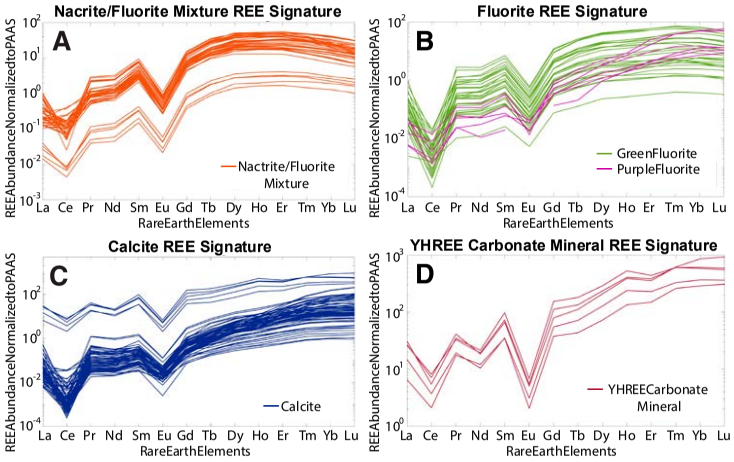

Figure11.(A)Rare-earthelement(REE)patternfornacriteandfluoritemixture;(B)REEpatternforgreenandpurplefluorite;(C)REEpatternforcalcite;and(D)REEpatternforyttriumandheavyrare-earthelement(YHREE)carbonatemineral.

5.DISCUSSION

5.1U-PbGeochronology

Thisstudyexplorestheutilityof U-Pbdatingoffluorite,nacrite,andcalcite paragenesisinREEmineralization.Giventheubiquitousoccurrenceofthesemineralsinhydrothermalsystems,U-Pbdatingholdsgreatpotentialforconstraining theageofassociatedoreminerals.Weusemultiplemicroscopytechniquesto investigatetherelationshipsbetweenfluorite,nacrite,andveinmineralization, andwecombinetheseobservationswithLA-ICP-MSelementmappingandU-Pb datingtoprovideabsolutetimeconstraintsonREEmineralization.

Animportantcontributionofthisworkisthatfluoriteandassociatednacrite arefaryoungerthanthetimeofigneouscrystallizationandthereforemusthave beendepositedbysecondaryfluids.Rare-earthelementoresareoften assumedtobedepositedduringlatestageigneouscrystallization.However, the6.2±2.8MafluoriteandnacriteagesstronglysuggestthatfluidsresponsibleformineralizationareassociatedwithRioGranderifting.Combining

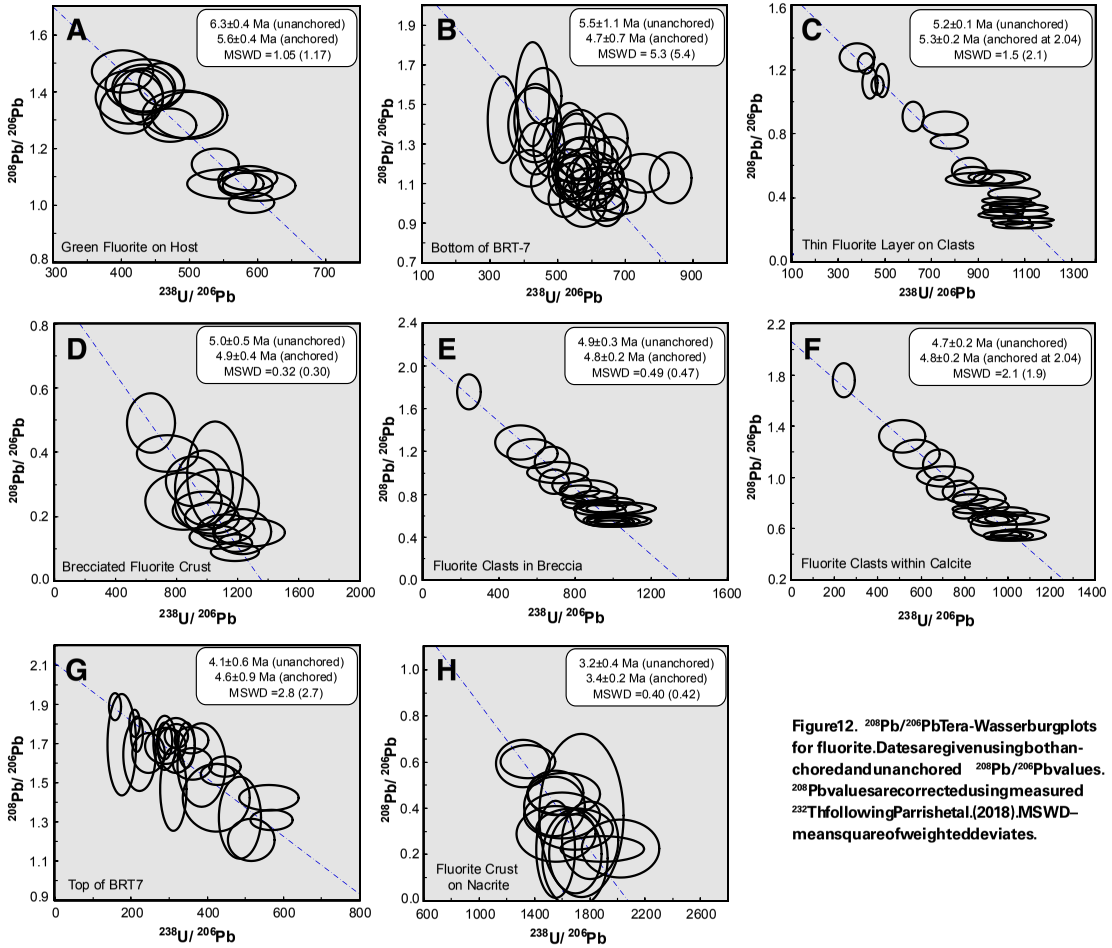

Figure12. $^{208}Pb/^{206}Pb$Tera-Wasserburgplots for fluorite.Datesaregivenusingbothan-choredandunanchored $^{208}Pb/^{206}Pb$values. ^{208}Pbvaluesarecorrectedusingmeasured ^{232}ThfollowingParrishetal.(2018).MSWD–meansquareofweighteddeviates.

geochronologicalevidencewiththeimagingtechniques,werecognizethe followingsequenceofeventsatRoundTop:(1)fracturingandalterationofthe hostrockwithdepositionoffl uoriteonfracturesurfaces;(2)furtherfracturingof hostrockandearlynacritedeposition,linedbyasecondgenerationoffl uorite, inthiscase,bothpurpleandgreen;(3)evenyoungernacriteandfl uoriteline veinswithinthefracturesandarecappedbygreenfl uoriteofthesameages; (4)brecciationofhostandveinmaterialwithevidenceofsomedissolutionof fluorite;(5)brecciaclastsarelinedbyaYHREEcarbonate;and(6)severalgen - erationsofcalcite,someofwhicharethemselveslinedbytheYHREEcarbonate (Fig.14).Thecalcitethatsurroundsbrecciaclastsdoesnothaveu-Pbratios thatallowustodateit,butbrowncalcitefoundinassociationwithitis1.7Ma (Fig.2H).NacritehashighREE,Th,andU,whilefl uoritehaslowREEwiththe samepattern,lowTh,andhighU.Thewhitecalcitethatpostdatestheyhree carbonatehasextremelyHREE-enrichedpatterns:upto1000× HREEconcen- trationsofpost-ArcheanAustralianshale(PAAS).Thedatedbrowncalcitehas lowREEconcentrations,andnoREEmineralsareobservedafteritsformation. Thus,REEmobilityisconstrainedtobebetween6.2and1.7Ma.

5.2MultipleFluidEventsoverthePast6.2Ma

The fluidresponsibleforearliestfractureveinmineralizationproducedan intimatemixtureofcryptocrystallinenacrite($Al_2Si_2O_5(OH)_4$)andfluorite.The presenceofnacritemaysuggesthydrothermalactivity,asithasbeenfound

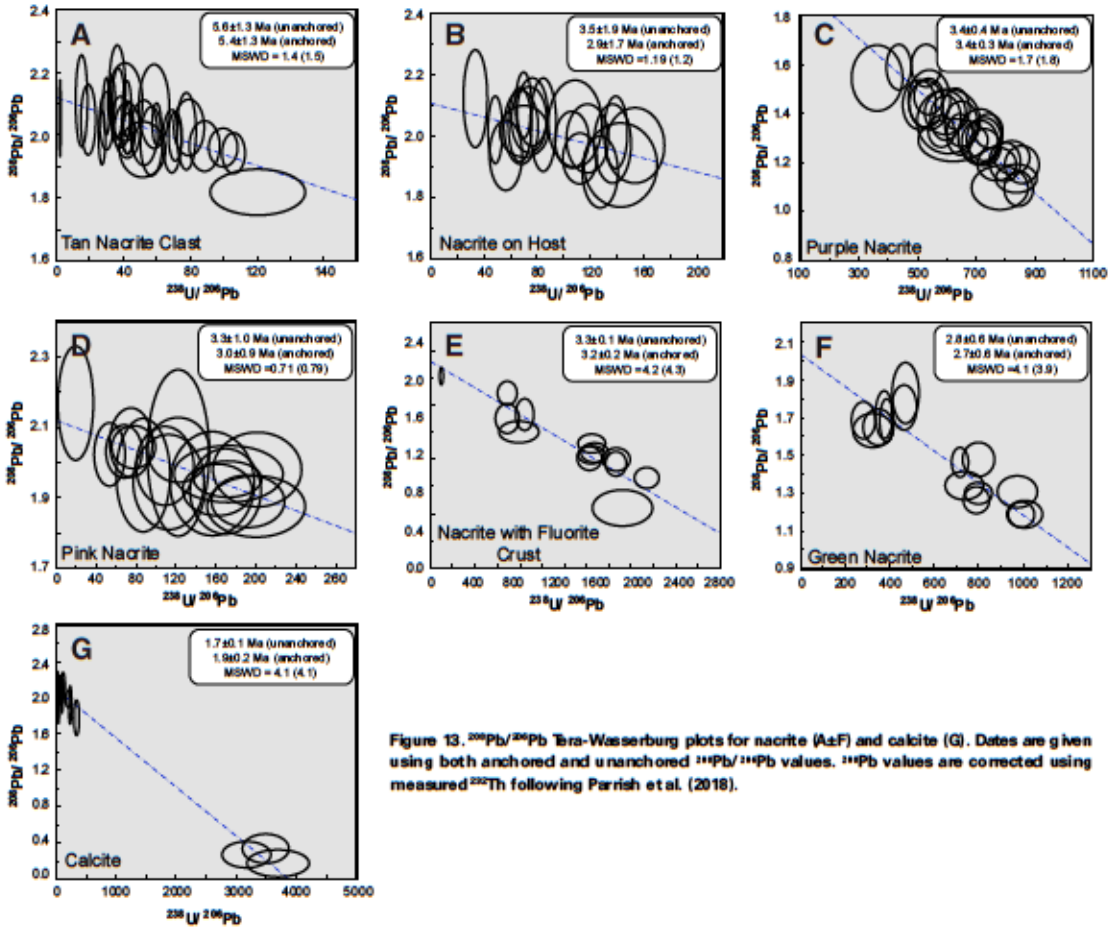

Figure 13. $^{208}Pb/^{206}Pb$ Tera-Wasserburg plots for nacrite (A±F) and calcite (G). Dates are given using both anchored and unanchored $^{208}Pb/^{206}Pb$ values. ^{208}Pb values are corrected using measured ^{232}Th following Parrish et al. (2018).

in association with hydrothermal fluorite in other areas (Polyakova, 1967). The presence of significant F in the fluid likely accounts for the solubility of Si and Al as well as the REE, U, and Th. As the fluid reached the fracture, changing conditions, such as seen with fault valves (Ramsay, 1980; Sibson, 1990) caused the precipitation of this nacrite/fluorite mix. The resulting deposit of nacrite/fluorite is enriched in U, Th, Y and REE suggesting that this fluid was a primary driver of trace element mobilization and enrichment. The close association between nacrite and fluorite suggests that this is a progression of precipitation from the same fluid event. U zoning within the fluorite suggests changing fluid conditions during mineral formation. REE patterns of nacrite and fluorite are similar to each other and show pronounced negative Ce and Eu anomalies, as well as enrichment of MREE-HREE relative to PAAS (or chondritic uniform reservoir [CHUR]) (Figs. 11A and 11B). The presence of a negative Ce anomaly is perhaps evidence that the fluid that deposited these minerals was highly oxidizing, which would have helped promote dissolution of primary minerals and trace-element mobilization. The negative Eu anomaly is similar to that measured by O'Neill et al. (2017) for the bulk Round Top rhyolite and is therefore not likely to be the result of fractionation in fluids related to vein mineralization. Fluorite has a range of ages from 6.2 to 3.2 Ma, with the earliest generation forming directly on the host rock. Later generations of fluorite clearly postdate nacrite and fluorite precipitation because these are always found capping the nacrite surface. The nacrite ranges in age from 5.6 to 2.8 Ma.

Brecciation of host rock, nacrite, and fluorite clearly demonstrates a later fluid event that likely accompanied fault movement. We find host rock and tan nacrite clasts lined by a purple fluorite that is 5.2 Ma. This fluorite has significantly greater HREE enrichment, relative to other REE, than any other

fluorite we analyzed (Fig. 11B) and occupies clast surfaces, similar to the mineralization of the YHREE mineral in later events. Fluorite and nacrite clasts ranging from 4.9 to 2.8 Ma are lined by an YHREE carbonate. A 4.1 Ma fluorite generation has resorption textures that demonstrate a fluid that was able to dissolve fluorite (Figs. 6, 9D, and 9E). It is not possible to say what caused the brecciation events, but many clasts have boundaries that clearly fit with neighboring clasts suggesting that some brecciation was in situ (Figs. 2B, 2C, and 2F). Importantly, these younger clasts are almost always lined by YHREE carbonate and are followed by white calcite with curved crystals. This calcite is depleted in LREE but is enriched HREE (Fig. 11C). We suggest that this YHREE mineral and calcite association is an evolution of precipitation from a fluid where the YHREE mineral is less soluble and precipitates first. The calcite growth could displace earlier minerals, but the brecciation must have occurred prior to the precipitation of the YHREE carbonate.

Clearly several distinct fluid events are recorded in Round Top veins. The fluorite and nacrite have a range of ages suggesting that a fluid with F was important from 6.2 to 2.8 Ma. Some of the fluorite has been brecciated and dissolved, demonstrating that a very different fluid chemistry followed fluorite mineralization. Finally, we see evidence for carbonate precipitation punctuated by multiple dissolution events that followed the brecciation events. Even with this complexity, two fluid types reasonably encompass the observations made: an early F-bearing fluid that resulted in multiple episodes of nacrite and fluorite precipitation, followed by one that dissolved fluorite and then precipitated carbonates presumably as it became saturated through mineral dissolution. However, what is less clear is the source of the REE. Rare-earth elements are highly enriched in nacrite and thus the first proposed fluid was able to mobilize REE. The REE patterns are enriched in the MREE and HREE with a pronounced positive hump across the MREEs (Fig. 11A). There are numerous REE-bearing minerals in the Round Top laccolith, and it is striking that one of the zircon generations shows abundant evidence for dissolution (Rubin et al., 1987; O'Neill et al., 2014, 2017). We hypothesize that the fluorine-bearing fluid was able to dissolve silicates and deliver the Al, Si, REE, and U to the veins. With the exception of the Ce anomaly, the REE pattern is similar to published patterns for zircons (O'Neill et al., 2017).

The second fluid can clearly dissolve fluorite as shown by resorption textures in vein fluorite. Given the oxidizing nature of this fluid, it is possible that it dissolved HREE-bearing yttrofluorite from the laccolith. Previous literature has suggested using sulfuric acid for dissolving yttrofluorite for extraction of REE (Pingitore et al., 2014; Negron et al., 2016). Within areas of the fluorite with evidence for dissolution, we see sulfur in close association with the YHREE carbonate (Fig. 9E). We speculate that the fluid was sulfuric acid bearing. A similar dissolution mechanism has been proposed in the Carlsbad area, where sulfuric acid is hypothesized to have been responsible for cavern formation in Permian carbonates (Davis, 1973; Jagnow, 1978; Davis, 1980; Hill, 1981). This sulfuric acid is thought to have resulted from Basin and Range uplift mobilizing oil and brines with associated H_2S that mixed with meteoric water as it neared the surface. Likewise, oxidation of sulfide minerals in wall rocks will also generate sulfuric acid. Regardless of the mechanism, uplift associated with Rio Grande rifting as well as Basin and Range faulting is important in the Trans-Pecos region and provides mechanisms for sulfuric acid formation.

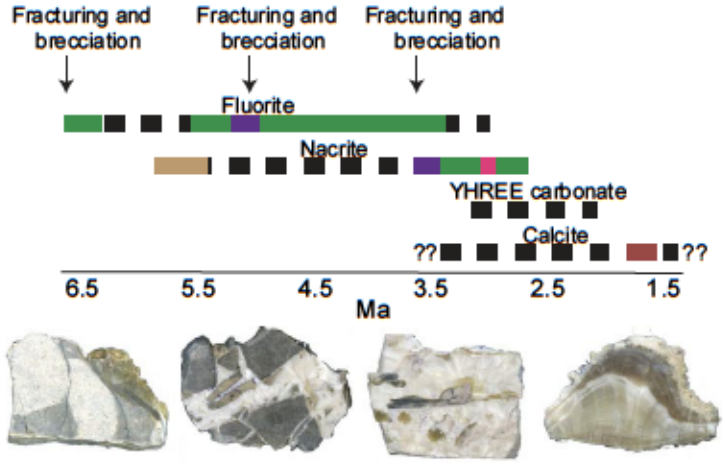

Figure 14. Paragenesis determined by the ages of fluorite, nacrite, and calcite. Each labeled line represents timing of crystallization of the specified mineral. Line colors represent mineralization color (i.e., purple = purple fluorite or purple nacrite crystallization). Dotted lines indicate undated (but possible) mineralization. Sample photos are representative of mineralization from 6.5 Ma to 1.5 Ma (going from left to right, decreasing in age). YHREE–yttrium heavy rare-earth element.

5.3 Round Top Vein Ages Match Period of Rio Grande Rift-Related Tectonism

To the north of Round Top, in the Bingham mine area of New Mexico, massive fluorite deposits in the Rio Grande rift have been attributed to a mantle source of fluorine (Partey et al., 2009). The ages for vein material at Round Top match the timing of a hiatus in Rio Grande rifting and a period of eastward tilting of the western Great Plains related to dynamic mantle upwelling (van Wijk et al., 2018). Across the Great Basin, there is a strong correlation between fluorine and transtensional tectonics (Holt et al., 2015, 2018). A recent synthesis of strain rates across the western United States demonstrates that the Rio Grande rift in the Trans Pecos region was under transtension between 12 and 4 Ma (Bahadori et al., 2018). The fluorite in the Bingham mine area has very low U and U-Pb and is not amenable to dating. Perhaps the difference at Round Top is that the fluid interacted with a U- and REE-enriched body. Based on the evolution of vein mineralization at Round Top, fluorine was important between 6.5 and 2.8 Ma, consistent with this being an interval of transtension in the Rio Grande rift. Magmatism of this age is not known in Trans-Pecos Texas (Henry and McDowell, 1986) and is limited and localized in the Rio Grande

rift in southern New Mexico (Aldrich et al., 1986). The results of radiometric dating of nacrite, fluorite, and calcite veins in this study suggest the potential to constrain episodes of transtensional tectonics and deep fluid input even in areas that lack contemporaneous magmatic bodies at the surface.

6. CONCLUSIONS

We show that there is great potential for LA-ICP-MS U-Pb dating of hydrothermal minerals to illuminate the timing of fluid events and to date associated ore deposits. At Round Top laccolith, we have evidence for multiple fluid events. Early fluid events have elevated REE with MREE-enriched patterns in nacrite and fluorite and range in age from 6.2 to 3.2 Ma. Later fluids brecciated and dissolved fluorite and nacrite and precipitated highly HREE-enriched carbonates: an YHREE carbonate followed by calcite. These minerals could not be directly dated but are bracketed by 2.8 Ma nacrite and a 1.7 Ma calcite that has low REE. The most important observation here is that the timing of mobilization greatly postdates igneous emplacement. Instead the timing is consistent with that of Rio Grande rifting. Fluorite deposits to the north in New Mexico are suggested to have a mantle source (Partey et al., 2009). Perhaps smaller amounts of fluorine fluxed through the Trans-Pecos area, mobilizing REE from various accessory minerals in the laccolith. It appears that an even more aggressive fluid followed that was capable of dissolving fluorides, the primary REE host in the laccolith, and brecciating the existing vein minerals and host rock. We speculate that this was a sulfuric acid±bearing fluid, perhaps due to mixing of H_2S-bearing brines with meteoric water, similar to that hypothesized for Carlsbad Caverns (Davis, 1973; Jagnow, 1978; Davis, 1980; Hill, 1981). A HREE carbonate and calcite were precipitated by this succeeding fluid. This fluid was followed by fluids that could both dissolve and precipitate calcite. A late generation of calcite with low REE but high U and U-Pb is dated at 1.7 Ma. We have not found evidence for REE mobilization that is later than this calcite generation.

This application of U-Pb dating of fluorite nacrite and elemental characterizing of a suite of vein minerals shows that this approach can be of use in future work understanding the geochemical processes that remobilize REE. More precise U-Pb geochronology on fluorite using LA-ICPMS could be of use in creating details chronologies of hydrothermal fluid events and ore mineralization.

ACKNOWLEDGMENTS, SAMPLES, AND DATA

We thank Perach Nuriel, Robert Holder, and editor Christopher Spencer for their constructive reviews and comments, which greatly improved the manuscript. The full data set beyond those published in this manuscript is available in Data Sets S1–S4, Supporting Information S1, and Table S1 (footnote 1). The authors declare no financial conflicts of interest. We thank Texas Mineral Resources Corporation for access to their Round Top property. Gavin Piccione was funded through a summer internship through Stony Brook University (SBU) Undergraduate Research and Creative Activities Program (URECA). Fieldwork (Piccione, Rasbury, and Jaret) was partially supported through a SBU Department of Geosciences fund from Rich Parrish. Additional support for field work was provided by the Ill Yager Professorship of the Jackson School of Geosciences (Kyle) and the State of Texas Advanced Resource Recovery (STARR) program through the University of Texas at Austin, Bureau of Economic Geology, Mineral Resource Program (Elliott). Summer 2018 undergraduate interns Nattarika Saengkhueankaeo (Ford) and Kevin Hatton who were supported by GEOPREP (National Science Foundation grant) provided some of the laser ablation data and initial data reduction. We thank Timothy Glotch (Stony Brook) for access and use of the Raman microscope. Wendy Austin-Giddings did the initial laser ablation analyses of sample BRT7 at NERC Isotope Geochronology Laboratory. Daniel Davis and William Holt have been involved in numerous discussions of the tectonic context that has helped to bring this research together. Aaron Celestian was involved in discussion and interpretation of XRD data. Portions of this work were performed at beamlines X15B and X26A of the National Synchrotron Light Source (NSLS), Brookhaven National Laboratory. X26A was supported by the Department of Energy (DOE) Geosciences (DE-FG02-92ER14244 to The University of Chicago, Center for Advanced Radiation Sources [CARS]). Use of the NSLS was supported by DOE under contract no. DE-AC02-98CH10886. Portions of this research were also performed at the Tender Energy Spectroscopy (TES), X-ray fluorescence microprobe (XFM), and submicron-resolution X-ray spectroscopy (SRX) beamlines and used resources of the National Synchrotron Light Source II, a U.S. Department of Energy (DOE) Office of Science User Facility operated for the DOE Office of Science by Brookhaven National Laboratory under contract no. DE-SC0012704. Construction of and work at the TES beamline and initial measurements at X15B were partly funded by the National Science Foundation±Earth Sciences (EAR-1128957), National Aeronautics and Space Association (NNX13AD12G), and the Department of Energy, Geosciences (DE-FG02-12ER16342). This research also used resources of the Advanced Photon Source, a U.S. Department of Energy (DOE) Office of Science User Facility operated for the DOE Office of Science by Argonne National Laboratory under contract no. DE-AC02-06CH11357. We acknowledge the support of GeoSoilEnviroCARS (Sector 13), which is supported by the National Science Foundation±Earth Sciences (EAR-1128799) and the Department of Energy, Geosciences (DE-FG02-94ER14466). Partial funding came from the National Science Foundation grant number EAR-1814091.

REFERENCES CITED

Aldrich, M.J., Chapin, C.E., and Laughlin, A.W., 1986, Stress history and tectonic development of the Rio Grande Rift, New Mexico: Journal of Geophysical Research, v. 91, p. 6199±6211, https://doi.org/10.1029/JB091iB06p06199.

Bahadori, A., Holt, W.E., and Rasbury, E.T., 2018, Reconstruction modeling of crustal thickness and paleotopography of western North America since 36 Ma: Geosphere, v. 14, no. 3, p. 1207±1231, https://doi.org/10.1130/GES01604.1.

Barker, D.S., 1987, Tertiary alkaline magmatism in Trans-Pecos Texas Early, *in* Fitton, J.G., and Upton, B.G.J., eds., Alkaline Igneous Rocks: Geological Society of London Special Publication 30, p. 415±431.

Bau, M., 1991, Rare-earth element mobility during hydrothermal and metamorphic fluid-rock interaction and the significance of the oxidation state of europium: Chemical Geology, v. 93, p. 219±230, https://doi.org/10.1016/0009-2541(91)90115-8.

Bau, M., and Dulski, P., 1995, Comparative study of yttrium and rare-earth element behaviours in fluorine-rich hydrothermal fluids: Contributions to Mineralogy and Petrology, v. 119, no. 2±3, p. 213±223, https://doi.org/10.1007/BF00307282.

Bau, M., and Moller, P., 1992, Rare earth element fractionation in metamorphogenic hydrothermal calcite, magnesite and siderite: Mineralogy and Petrology, v. 45, p. 231±246, https://doi.org/10.1007/BF01163114.

Burisch, M., Walter, B.F., and Markl, G., 2017, Silicification of hydrothermal gangue minerals in Pb-Zn-Cu-fluorite-quartz-baryte veins: The Canadian Mineralogist, v. 55, no. 3, p. 501±514, https://doi.org/10.3749/canmin.1700005.

C novas, C.R., Madías, F., Llópez, R.P., and Nieto, J.M., 2018, Mobility of rare earth elements, yttrium and scandium from a phosphogypsum stack: Environmental and economic implications: The Science of the Total Environment, v. 618, p. 847±857, https://doi.org/10.1016/j.scitotenv.2017.08.220.

Davis, D.G., 1973, Sulfur in Cottonwood Cave, Eddy County, New Mexico: Bulletin of the National Speleological Society, v. 35, no. 3, p. 89±95.

Davis, D.G., 1980, Cave development in the Guadalupe Mountains: A critical review of recent hypotheses: The NSS Bulletin, v. 42, no. 3, p. 42±48.

Debruyne, D., Hulsbosch, N., and Muchez, P., 2016, Unraveling rare earth element signatures in hydrothermal carbonate minerals using a source-sink system: Ore Geology Reviews, v. 72, p. 232±252, https://doi.org/10.1016/j.oregeorev.2015.07.022.

Elliott, B.A., 2018, Petrogenesis of heavy rare earth element enriched rhyolite: Source and magmatic evolution of the Round Top laccolith, Trans-Pecos, Texas: Basel, Switzerland, Minerals, v. 8, no. 10, p. 423, https://doi.org/10.3390/min8100423.

Fan, H., Xie, Y., Wang, K., Tao, K., and Wilde, S.A., 2004, REE daughter minerals trapped in fluid inclusions in the Giant Bayan Obo REE-Nb-Fe deposit, inner Mongolia, China: International Geology Review, v. 46, p. 638±645, https://doi.org/10.2747/0020-6814.46.7.638.

Genna, D., Gaboury, D., and Roy, G., 2014, Evolution of a volcanogenic hydrothermal system recorded by the behavior of LREE and Eu: Case study of the Key Tuffite at Bracemac-McLeod deposits, Matagami, Canada: Ore Geology Reviews, v. 63, p. 160±177, https://doi.org/10.1016/j.oregeorev.2014.04.019.

Gierth, R., 1990, Hydrothermal mobility of Ti, Zr and REE: Examples from the Bergell and Adamello contact aureoles (Italy): Terra Nova, v. 2, p. 60±67, https://doi.org/10.1111/j.1365-3121.1990.tb00037.x.

Henry, C.D., and McDowell, F.W., 1986, Geochronology of magmatism in the Tertiary volcanic field, Trans-Pecos Texas, *in* Price, J.G., Henry, C.D., Parker, D.F., and Barker, D.S., eds., Texas: Igneous Geology of Trans-Pecos Texas: Texas Bureau of Economic Geology, University of Texas at Austin, Guidebook 23, p. 99±122.

Henry, C.D., and Price, J.G., 1984, Variations in Caldera Development in the Tertiary Volcanic Field of Trans-Pecos Texas: Journal of Geophysical Research, v. 89, p. 8765±8786, https://doi.org/10.1029/JB089iB10p08765.

Henry, C.D., Price, J.G., and Miser, D.E., 1989, Geology and Tertiary igneous activity of the Hen Egg Mountain and Christmas Mountains Quadrangles, Big Bend region: Trans-Pecos, Texas: Bureau of Economic Geology, University of Texas at Austin, https://doi.org/10.23867/RI0183D.

Hill, C.A., 1981, Speleogenesis of Carlsbad Caverns and other caves in the Guadalupe Mountains: Bowling Green, Kentucky, Proceedings of the International Congress of Speleology, p. 143±144.

Holt, W.E., Rasbury, T., Wang, X., and Piccione, G.G., 2015, A measured correlation between fluorine concentrations in geothermal springs and Great Basin crustal strain rates: A new geochemical tracer for mantle fluid input: Geological Society of America Abstracts with Programs, v. 47, no. 7, p. 818.

Holt, W.E., Rasbury, T., Bahadori, A., Shen, W., and Kim, J., 2018, Fluorine concentrations in geothermal springs as an indicator of rheological weakening promoting active deformation in Western North America: American Geophysical Union abstract #T21G-0319.

Horstwood, M.S.A., Ko, J., Gehrels, G., Jackson, S.E., Mclean, N.M., Paton, C., and Schoene, B., 2016, Community-derived standards for LA-ICP-MS U-(Th-) Pb geochronology–uncertainty propagation, age interpretation and data reporting: Geostandards and Geoanalytical Research, v. 40, p. 311±332, https://doi.org/10.1111/j.1751-908X.2016.00379.x.

Jagnow, D.H., 1978, Geology and speleogenesis of Ogle Cave, New Mexico: Bulletin of the National Speleological Society, v. 40, no. 1, p. 7±18.

Lanzirotti, A., Tappero, R., and Schulze, D.G., 2010, Practical application of synchrotron-based hard X-ray microprobes in soil sciences, *in* Singh, B., and Grafe, M., eds., Synchrotron-Based Techniques in Soils and Sediments: Developments in Soil Science, v. 34: Elsevier, p. 27±72, https://doi.org/10.1016/S0166-2481(10)34002-5.

Li, Xian-hua, Liu, D., Sun, M., Li, W., Liang, X.-R., and Liu, Y., 2004, Precise Sm-Nd and U-Pb isotopic dating of the supergiant Shizhuyuan polymetallic deposit and its host granite, SE China: Geological Magazine, v. 141, p. 225±231, https://doi.org/10.1017/S0016756803008823.

Li, Xiaochun, and Zhou, M., 2015, Multiple stages of hydrothermal REE remobilization recorded in fluorapatite in the Paleoproterozoic Yinachang Fe-Cu-(REE) deposit, Southwest China: Geochimica et Cosmochimica Acta, v. 166, p. 53±73, https://doi.org/10.1016/j.gca.2015.06.008.

Lottermoser, B.G., 1992, Rare earth elements and hydrothermal ore formation processes: Ore Geology Reviews, v. 7, no. 1, p. 25±41, https://doi.org/10.1016/0169-1368(92)90017-F.

Ludwig, K.R., 1998, On the treatment of concordant uranium-lead ages: Geochimica et Cosmochimica Acta, v. 62, no. 4, p. 665±676, https://doi.org/10.1016/S0016-7037(98)00059-3.

Ludwig, K.R., 2003, User's manual for a geochronological toolkit for Microsoft Excel (Isoplot/Ex version 3.0): Berkeley Geochronology Center Special Publication No. 4.

Ludwig, K.R., 2012, User's Manual for Isoplot 3.75: A Geochronological Toolkit for Microsoft Excel: Berkeley Geochronology Center Special Publication No. 5.

Muehlberger, W.R., 1980, Texas lineament revisited, *in* Trans-Pecos region, southeastern New Mexico and west Texas: New Mexico Geological Society Fall Field Conference Guidebook, v. 31, p. 113±121.

Negron, L., Pingitore, N., and Gorski, D., 2016, Porosity and permeability of Round Top Mountain rhyolite (Texas, USA) favor coarse crush size for rare earth element heap leach: Minerals, v. 6, p. 16, https://doi.org/10.3390/min6010016.

Ngwenya, T.B., 1994, Hydrothermal rare earth mineralisation in carbonatites of the Tundulu complex, Malawi: Processes at the fluid/rock interface: Geochimica et Cosmochimica Acta, v. 58, no. 9, p. 2061±2072, https://doi.org/10.1016/0016-7037(94)90285-2.

Northrup, P., 2019, The TES beamline (8-BM) at NSLS-II : Tender-energy spatially resolved X-ray absorption spectroscopy and X-ray fluorescence imaging: Journal of Synchrotron Radiation, v. 26, https://doi.org/10.1107/S1600577519012761.

Northrup, P., Leri, A., and Tappero, R., 2016, Applications of "tender" energy (1-5 keV) X-ray absorption spectroscopy in life sciences: Protein and Peptide Letters, v. 23, p., http://doi.org/10.2174/0929866523666160107114505.

O'Neill, L.C., Kyle, J.R., and Elliott, B., 2014, REE-Be-U-F Enriched Mineralization of the Round Top Laccolith, Sierra Blanca Peaks, Trans-Pecos Texas [Master's thesis]: Austin, Texas, The University of Texas at Austin.

O'Neill, L.C., Elliott, B.A., and Kyle, J.R., 2017, Mineralogy and crystallization history of a highly differentiated REE-enriched hypabyssal rhyolite: Round Top laccolith, Trans-Pecos, Texas: Mineralogy and Petrology, v. 111, no. 4, p. 569±592, https://doi.org/10.1007/s00710-017-0511-5.

Parrish, R.R., Parrish, C.M., and Lasalle, S., 2018, Vein calcite dating reveals Pyrenean orogen as cause of Paleogene deformation in southern England: Journal of the Geological Society, v. 175, https://doi.org/10.1144/jgs2017-107.

Parsley, F., Lev, S., Casey, R., Widom, E., Lueth, V.W., and Rakovan, J., 2009, Source of fluorine and petrogenesis of the Rio Grande Rift-type barite-fluorite-galena deposits: Economic Geology and the Bulletin of the Society of Economic Geologists, v. 104, p. 505±520, https://doi.org/10.2113/gsecongeo.104.4.505.

Paton, C., Hellstrom, J., Paul, B., Woodhead, J., and Hergt, J., 2011, Iolite: Freeware for the visualisation and processing of mass spectrometric data: Journal of Analytical Atomic Spectrometry, v. 26, p. 2508±2518, https://doi.org/10.1039/c1ja10172b.

Pfaff, K., Romer, R.L., and Markl, G., 2009, U-Pb ages of ferberite, chalcedony, agate, "U-mica" and pitchblende: Constraints on the mineralization history of the Schwarzwald ore district: European Journal of Mineralogy, v. 21, no. 4, p. 817±836, https://doi.org/10.1127/0935-1221/2009/0021-1944.

Pingitore, N., Clague, J., and Gorski, D., 2014, Round Top Mountain rhyolite (Texas, USA), a massive, unique Y-bearing-fluorite-hosted heavy rare earth element (HREE) deposit: Journal of Rare Earths, v. 32, no. 1, p. 90±96, https://doi.org/10.1016/S1002-0721(14)60037-5.

Polyakova, O.P., 1967, Nacrite from the fluorite deposits of Eastern Transbaykalia: International Geology Review, v. 9, p. 225±229, https://doi.org/10.1080/00206816709474459.

Ponnurangam, A., Bau, M., Brenner, M., and Koschinsky, A., 2015, Mussel shells of Mytilus edulis as bioarchives of the rare earth elements and yttrium distribution in seawater and the potential impact of pH and temperature on the partitioning behaviour: Biogeosciences Discussions, v. 12, no. 17, p. 14911±14939, https://doi.org/10.5194/bgd-12-14911-2015.

Price, J.G., Henry, C.D., Barker, D.S., and Parker, D.F., 1987, Alkalic rocks of contrasting tectonic settings in Trans-Pecos Texas, *in* Morris, E.M., and Pasteris, J.D., eds., Mantle Metasomatism and Alkaline Magmatism: Geological Society of America Special Paper 215, p. 335±346, https://doi.org/10.1130/SPE215-p335.

Price, J.G., Rubin, J.N., Henry, C.D., Pinkston, T.L., Tweed, S.W., and Koppenaal, D.W., 1990, Rare-metal enriched peraluminous rhyolites in a continental arc, Sierra Blanca area, Trans-Pecos Texas: Chemical modification by vapor-phase crystallization, *in* Stein, H.J., and Hannah, J.L., eds., Ore-Bearing Granite Systems; Petrogenesis and Mineralizing Processes: Geological Society of America Special Paper 246, p. 103±120 https://doi.org/10.1130/SPE246-p103.

Ramsay, J.G., 1980, The crack-seal mechanism of rock deformation: Nature, v. 284, p. 135±139, https://doi.org/10.1038/284135a0.

Ricketts, J.W., Kelley, S.A., Karlstrom, K.E., Schmandt, B., and Donahue, M.S., 2016, Synchronous opening of the Rio Grande rift along its entire length at 25±10 Ma supported by apatite (U-Th)/He and fission-track thermochronology, and evaluation of possible driving mechanisms: Geological Society of America Bulletin, v. 128, no. 3/4, p. 397±424, https://doi.org/10.1130/B31223.1.

Roberts, N.M.W., Rasbury, E.T., Parrish, R.R., Horstwood, M.S.A., Condon, D.J., and Smith, C.J., 2017, A calcite reference material for LA-ICP-MS U-Pb geochronology: Geochemistry, Geophysics, Geosystems, v. 18, p. 2807±2814, https://doi.org/10.1002/2016GC006784.

Rowe, M.C., Lassiter, J.C., and Goff, K., 2015, Basalt volatile fluctuations during continental rifting: An example from the Rio Grande Rift, USA: Geochemistry, Geophysics, Geosystems, v. 16, p. 1254±1273, https://doi.org/10.1002/2014GC005649.

Rubin, J.N., Price, J.G., Henry, C.D., and Koppenaal, D.W., 1987, Cryolite-bearing and rare metal-enriched rhyolite, Sierra Blanca Peaks, Hudspeth County, Texas: The American Mineralogist, v. 72, no. 11±12, p. 1122±1130.

Rubin, J.N., Henry, C.D., and Price, J.G., 1993, The mobility of zirconium and other "immobile" elements during hydrothermal alteration: Chemical Geology, v. 110, p. 29–47, https://doi.org/10.1016/0009-2541(93)90246-F.

Shannon, W.M., 1986, Lithogeochemical characterization of intrusive rocks comprising the Quitman-Sierra Blanca igneous complex, Hudspeth County, Texas [M.S. thesis]: University of Texas at El Paso, https://digitalcommons.utep.edu/dissertations/AAIEP02340.

Shannon, W.M., and Goodell, P.C., 1986, Lithogeochemistry of intrusive rocks of the Quitman-Sierra Blanca igneous complex, Hudspeth County, *in* Price, J.G., Henry, C.D., Parker, D.F., and Barker, D.S., eds., Texas: Igneous Geology of Trans-Pecos Texas: Texas Bureau of Economic Geology, University of Texas at Austin, Guidebook 23, p. 225–226.

Sheard, E.R., Williams-Jones, A.E., Heiligmann, M., Pederson, C., and Trueman, D.L., 2012, Controls on the concentration of zirconium, niobium, and the rare earth elements in the Thor Lake Rare Metal Deposit, Northwest Territories, Canada: Economic Geology and the Bulletin of the Society of Economic Geologists, v. 107, no. 1, p. 81–104, https://doi.org/10.2113/econgeo.107.1.81.

Sibson, R.H., 1990, Conditions for fault-valve behaviour, *in* Knipe, R.J., and Rutter E.H., eds., Deformation Mechanisms, Rheology and Tectonics: Geological Society of London Special Publication 54, p. 15–28, https://doi.org/10.1144/GSL.SP.1990.054.01.02.

Tan, S., Zhou, J., Li, B., and Zhao, J., 2017, In situ Pb and bulk Sr isotope analysis of the Yinchanggou Pb-Zn deposit in Sichuan Province (SW China): Constraints on the origin and evolution of hydrothermal fluids: Ore Geology Reviews, v. 91, p. 432–443, https://doi.org/10.1016/j.oregeorev.2017.09.012.

van Dongen, M., Weinberg, R.F., and Tomkins, A.G., 2010, REE-Y, Ti, and P remobilization in magmatic rocks by hydrothermal alteration during Cu-Au deposit formation: Economic Geology and the Bulletin of the Society of Economic Geologists, v. 105, no. 4, p. 763–776, https://doi.org/10.2113/gsecongeo.105.4.763.

van Wijk, J., Koning, D., Axen, G., Coblentz, D., Gragg, E., and Sion, B., 2018, Tectonic subsidence, geoid analysis, and the Miocene–Pliocene unconformity in the Rio Grande rift, southwestern United States: Implications for mantle upwelling as a driving force for rift opening: Geosphere, v. 14, p. 684–709, https://doi.org/10.1130/GES01522.1.

Walter, B.F., Gerdes, A., Kleinhanns, I.C., Von Eynatten, H., Kreissl, S., and Markl, G., 2018, The connection between hydrothermal fluids, mineralization, tectonics and magmatism in a continental rift setting: Fluorite Sm-Nd and hematite and carbonates U-Pb geochronology from the Rhinegraben in SW Germany: Geochimica et Cosmochimica Acta, v. 240, p. 11–42, https://doi.org/10.1016/j.gca.2018.08.012.

Williams-Jones, A.E., Migdisov, A.A., and Samson, I.M., 2012, Hydrothermal mobilisation of the rare earth elements–A tale of "ceria" and "yttria": Elements, v. 8, no. 5, p. 355–360, https://doi.org/10.2113/gselements.8.5.355.

Yang, F., Wang, G., Cao, H., Li, R., Tang, L., Huang, Y., Zhang, H., Xue, F., Jia, W., and Guo, N., 2017, Geoscience frontiers timing of formation of the Hongdonggou Pb-Zn polymetallic ore deposit, Henan Province, China: Evidence from Rb-Sr isotopic dating of sphalerites: Geoscience Frontiers, v. 8, no. 3, p. 605–616, https://doi.org/10.1016/j.gsf.2016.06.001.